Thermal Transport across Membranes and the Kapitza Length from Photothermal Microscopy

Panagis D. Samolis¹, Michelle Y. Sander^{1,4,5}, Mi K. Hong³, Shyamsunder Erramilli*^{3,4,5}, Onuttom Narayan*⁶

Departments of Electrical Engineering¹, Chemistry², Physics³, Biomedical Engineering⁴ and The Photonics Center⁵, Boston University, Boston, MA 02215, United States

⁶Department of Physics, University of California Santa Cruz, Santa Cruz CA, United States

* Please address correspondence to shyam@bu.edu or onarayan@uscc.edu

Abstract

An analytical model is presented for light scattering associated with heat transport near a cell membrane that divides a complex system into two topologically distinct half spaces. Our analysis is motivated by experiments on Vibrational Photothermal microscopy which have not only demonstrated remarkably high contrast and resolution, but also are capable of providing label-free local information of heat transport in complex morphologies. In the first-Born approximation, the derived Green's function leads to the reconstruction of a full 3D image with photothermal contrast obtained using both amplitude and phase detection of periodic excitations. We show that important fundamental parameters including the Kapitza length and Kapitza resistance can be derived from experiments. Our goal is to spur additional experimental studies with high frequency modulation and heterodyne detection in order to make contact with recent theoretical molecular dynamics calculations of thermal transport properties in membrane systems.

Keywords: Photothermal, Thermal Transport, Cell membranes, Kapitza Length, Kapitza Resistance

1. Introduction

Photothermal microscopy involves a general principle that has been observed for millennia, namely that thermal modulation can influence the scattering of light. A fascinating history of experiments dating back to the nineteenth century¹ led to ingenious innovations. After the invention of the laser the prospects of methods for generating contrast and imaging were enhanced, but the method was largely ignored by the microscopy community until the start of the new millennium when a series of remarkable papers²,³ demonstrated stunning contrast competitive with fluorescence label-based methods with a signal-tonoise sufficient to detect single molecules⁴,⁵. Extensions of the method to the mid-infrared region of the electromagnetic spectrum enabled by the development of Quantum Cascade Lasers⁶ and enhanced

heterodyne detection methods^{7,8,9,10}, have matured to the point of super-resolution down to hundreds of nanometers^{11,9,10} and detecting features as small as 50 nm⁸. Other advances include imaging of living cells⁹ and single viruses^{12,13}, as well as performing ultrafast widefield chemical imaging^{14,15}, quantitative phase imaging 16,17, improved imaging quality via fluorescence detection 18 and photothermal dynamic imaging with nanosecond resolution¹⁹. The interplay between elastic scattering of the probe beam and the absorbing pump beam is well understood at least in the context of linear spectroscopy. There is also the regime of non-linear photothermal methods^{6,7,20} that should be noted and that remains a less explored field where localized phase transitions and the formation of nanobubbles play a critical role in increased signal and resolution. Photothermal microscopy based methods can provide not only contrast originating from induced absorption and chemical composition but also information regarding thermal transport properties²¹ that do not require any incorporation of a temperature sensing probe. Contrast from varying thermal diffusion properties has been demonstrated using Vibrational Infrared Photothermal and Phase Signal (VIPPS) methodology²² and other ultrafast chemical imaging methods including nanosecond MHz digitization and match filtering¹⁹. The ability to map heat diffusion can have applications in various fields including semiconductor transport²³, thermal transport in plasmonic nanoparticle-solvent systems, and in reduced dimensional systems, including quasi 1D systems like biological fibrils and 2D systems like graphene.

There is a lot of interest and discussion regarding heat diffusion processes in biological systems across membranes and down to the intracellular level^{24,25}. The importance of understanding non-equilibrium heat transport in cells presents the need for both theoretical studies as well as experimental work. New theoretical arguments for entropy and energy associated with metabolic processes at the single cell level have been presented as well as new experimental methods based on nanodiamonds for local thermometry^{26,27} as well as fluorescent markers²⁸. All this can spur further theoretical models informed by molecular dynamics^{29,30}. However, the question of heat and energy transport across cell membranes has not been studied as closely, especially in terms of increased thermal resistivity. Partly this may have been because most works have been quasi-equilibrium studies at a fixed temperature. Various theoretical studies on the thermal properties of polymer chains^{31,32}, the Kapitza length of protein-water³³ interfaces and lipid bilayers^{30,34} have been proposed, with transport exponents suggesting a role for underlying fractal transport geometries, with predictions of thermal property values that suggest an increased thermal resistivity across such boundaries compared to water. Experimental work with upcoming nanothermometry on lipid bilayers³⁵ also provides some support for this idea. Other studies suggest that the presence of transmembrane proteins can cause membrane perturbations³⁶ which should impact the thermal properties as well. Even though increased membrane resistivity has been suggested in the past³⁷ in photothermal work, there has been little experimental or theoretical work to demonstrate the effect from the lens of photothermal measurements, especially in the realm of mid-infrared. On the theoretical front, there has been considerable recent interest in non-Fourier heat conduction models since the pioneering work of Tzou³⁸ exemplified by dual-phase lag models in heterogeneous tissue, taking convective and memory effects into account. A critical review of lagging heat models summarizes the progress made³⁹. How to best relate dual-phase lag model and enhanced continuum models to Molecular Dynamics Simulation estimates of the Kapitza length in membrane lipid-water systems remains an unsolved open question.

Previous experimental work using VIPPS microscopy has shown high contrast from membrane boundaries based on the phase signal measured in lock-in detection²². Similar lock-in detection of amplitude and phase signals has been demonstrated in photothermal radiometry for high frequency measurements of

Kapitza resistance in titanium coatings⁴⁰. Legrand et al²⁴ have developed a thermo-acoustic method using both phase and amplitude thermal images to map thermal properties and effusivity of single cells, reporting a cell effusivity of $E_{cell} \approx 2.6 \times 10^3 \mathrm{W \cdot m^{-2} K^{-1} s^{1/2}}$. Nano-sized cell membranes act as thermal barriers, and VIPPS offers a combination of chemical imaging and thermal diffusion characterization that paves the way towards label-free imaging of cell models and tissues and the transport of heat.

It is this broader emerging context of studying how thermal resistivity can enhance contrast in photothermal imaging that our paper addresses. In this work a tractable analytical model is presented along with finite difference time domain simulations of heat transfer across such barriers. Our goal is to suggest that photothermal heterodyne detection can be further expanded to provide information about thermal transport across cell membranes and heterogeneous material boundaries. In addition our simulations aim to motivate new experimental work that can enable detection of nano-size membranes as well as validate recent calculations of the Kapitza length in cell membranes. A very interesting question worthy of study in its own right is whether such an enhanced contrast will also persist in regimes different from the one studied in this paper, where non-Fourier bioheat models are applicable.³⁹

2. Model

As a representative numerical model system, an infinite plane cell membrane in the xy plane with two different regions in which heat propagates diffusively was chosen (Figure 1). The medium on both sides of the cell membrane can vary, and accordingly we allow the diffusion constants on the two sides of the membrane to be different. The cell membrane itself has a thermal resistance. Periodic heating pulses are applied to a localized region on one side of the cell membrane, and the temperature in the vicinity of this region is raised as a result. The infinite plane approximation for the cell membrane should be valid if the region where heating occurs, and the distance of this region from the membrane, is small compared to the local radius of curvature of the membrane. An extension to a spherical membrane in 3D is also presented that validates the infinite plane approximation.

Validity of the Diffusive transport model: The model described below is the simplest standard heat transfer model, and has been widely used in prior literature. Such models have limitations in applications to bioheat transfer in heterogeneous tissue and other semiconductor systems, highlighted in recent reviews and papers on non-Fourier mechanisms of heat transport, as convective and hydrodynamic effects are not included in simple diffusive models. There are two necessary conditions on space and time: (i) the mean free path must be smaller than the length scale over which the temperature varies by an experimentally measurable value; (ii) the mean time between collisions must be shorter than the time scale over which the temperature varies by an experimentally measurable value. As we show in the SI, in liquid water the mean free path from kinetic theory and MD simulations is $\langle \lambda_{\rm mfp} \rangle \simeq 0.2$ nm and the mean time between collisions is $\langle \tau_{\rm coll} \rangle \simeq 10^{-14} {\rm s}$. In the photothermal experiments using a Quantum Cascade Laser system, the mid-IR pulse widths are around hundreds of ns, with a repetition rate of the QCL of 100 MHz or less. All the length scales in our system are $^{\sim}$ 10 nm or larger. Thus both the necessary conditions are comfortably satisfied for our analytical model as well as the simulations, justifying the neglect of hydrodynamic effects.

In addition, there can be convective effects, which are of importance in bioheat tissue models with blood perfusion. In the particular system we study here, convective effects are negligible. The Peclet number is $\text{Pe} \ll 1$ indicating that advective transport in negligible and diffusive transport dominates. In MD simulations too, on the length scales studied in various ensembles convection near lipid boundaries $^{30~42}$ is not considered.

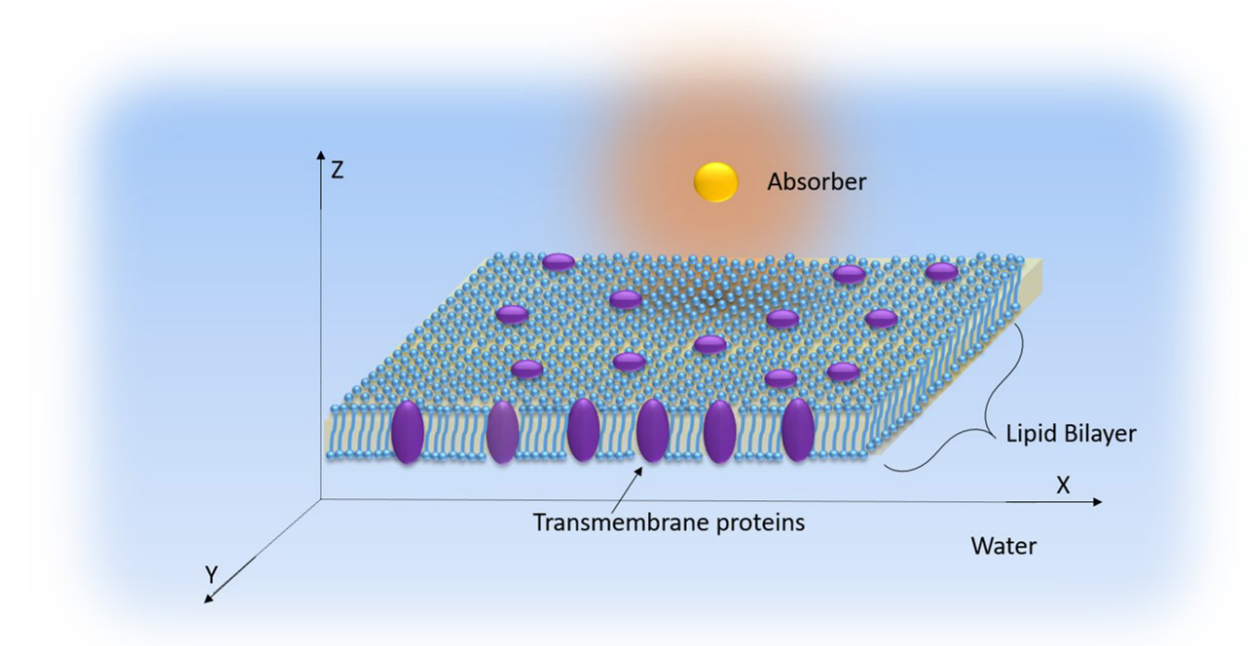


Figure 1: Illustration of a single absorber distanced 30 nm from a cell membrane model of lipid bilayers containing transmembrane proteins located at z = 0.

2.1. Sinusoidal Heating:

For the analytical model, we start with the fundamentals and first consider the heat equation for the case when the heating occurs at a point, and varies sinusoidally with time:

$$\frac{\partial T}{\partial t} = D_{+} \nabla^{2} T + \delta(z - a) \delta(x) \delta(y) e^{-i\omega t} \qquad z > 0$$

$$\frac{\partial T}{\partial t} = D_{-} \nabla^{2} T \qquad z < 0 \qquad (1)$$

Here $T(\mathbf{r},t)$ is the temperature. D_+ is the thermal diffusion constant and C_+ is the specific heat for z>0 with D_- being the thermal diffusion constant and C_- the specific heat for z<0. The excess energy density above the thermal equilibrium density in the two regions is then equal to $C_\pm T$ so that the associated heat current is equal to $C_\pm D_\pm \nabla T$. Accordingly, the matching condition across the z=0 interfacial plane is

$$D_{+}C_{+}\frac{\partial T}{\partial z}\Big|_{z=0^{+}} = D_{-}C_{-}\frac{\partial T}{\partial z}\Big|_{z=0^{-}} = \frac{1}{\rho}[T(z=0^{+}) - T(z=0^{-})]$$
 (2)

where ρ is the thermal resistance per unit area. The parameter $L_{K+} \equiv \rho D_+ C_+$ with units of length is called the Kapitza length associated with the boundary with the z > 0 region.

$$T(\mathbf{r},t) = T_{\omega}(\mathbf{r})e^{-i\omega t}$$
 (3)

The two equations in Eq.(1) are equivalent to

$$(-i\omega - D_{+}\nabla^{2})T_{\omega}(\mathbf{r}) = \delta(z - a)\delta(x)\delta(y) \qquad z > 0$$
$$(-i\omega - D_{-}\nabla^{2})T_{\omega}(\mathbf{r}) = 0 \qquad z < 0 \tag{4}$$

Fourier transforming the temperature in the xy plane

$$T_{\omega}(\mathbf{r}) = \int T_{\omega}(\mathbf{q}_{\perp}, z)e^{i\mathbf{q}_{\perp} \cdot \mathbf{r}} \frac{d^2 q_{\perp}}{4\pi^2}$$
 (5)

we obtain

$$(D_{+}q_{\perp}^{2} - i\omega)T_{\omega}(\mathbf{q}_{\perp}, z) - D_{+}\frac{\partial^{2}T_{\omega}(\mathbf{q}_{\perp}, z)}{\partial z^{2}} = \delta(z - a) \qquad z > 0$$

$$(D_{-}q_{\perp}^{2} - i\omega)T_{\omega}(\mathbf{q}_{\perp}, z) - D_{-}\frac{\partial^{2}T_{\omega}(\mathbf{q}_{\perp}, z)}{\partial z^{2}} = 0 \qquad z < 0 \qquad (6)$$

with Eq.(2) unchanged except for the fact that $T(\mathbf{r},t)$ has been replaced by $T_{\omega}(\mathbf{q}_{\perp},z)$ This is a standard one-dimensional Green's function problem; \mathbf{q}_{\perp} can be treated as a parameter, and suppressed as an argument of $T_{\omega}(\mathbf{q}_{\perp},z)$ to make the notation more compact in the following.

The solution to the equation is of the form

$$T_{\omega}(z < 0) = Ae^{\kappa_{-}z}$$

$$T_{\omega}(z > 0) = Fe^{-\kappa_{+}z} + \frac{1}{2D_{+}\kappa_{+}}e^{-\kappa_{+}|z-a|}$$
(7)

where

$$\kappa_{\pm} = \sqrt{q_{\perp}^2 - \frac{i\omega}{D_{\pm}}} \tag{8}$$

with the square root chosen to have a positive real part. The second term in $T_{\omega}(z>0)$ is what one would have obtained without the boundary at z=0 while the other terms in Eq.(7) are 'image' terms for z<0 and z>0.

Now applying the boundary conditions at z = 0,

$$\kappa_{-}C_{-}D_{-}A = -\kappa_{+}C_{+}D_{+}F + \frac{1}{2}C_{+}e^{-\kappa_{+}a}$$

$$\kappa_{-}C_{-}D_{-}A = \frac{1}{\rho}\left(\frac{1}{2D_{+}\kappa_{+}}e^{-\kappa_{+}a} + F - A\right)$$
(9)

from which

$$A = (\kappa_{-}C_{-}D_{-}\kappa_{+}C_{+}D_{+}\rho + \kappa_{+}C_{+}D_{+} + \kappa_{-}C_{-}D_{-})^{-1}C_{+}e^{-\kappa_{+}a}$$

$$F = \frac{1}{2}A\left(\kappa_{-}C_{-}D_{-}\rho + 1 - \frac{\kappa_{-}C_{-}D_{-}}{\kappa_{+}C_{+}D_{+}}\right)$$
(10)

Thus all the parameters in Eq.(7) have been determined.

2.2. Space time temperature profile pulse response

If heat is applied sinusoidally, one can obtain $T(\mathbf{q}_{\perp},z,t)$ from $T_{\omega}(\mathbf{q}_{\perp},z)$ by multiplying a factor of $e^{-i\omega t}$. If heat is applied as a series of equally spaced pulses instead of as a sinusoidal function of time, the first equation in Eq.(1) is changed while the second remains the same

$$\frac{\partial T}{\partial t} = D_{+} \nabla^{2} T + \delta(z - a) \delta(x) \delta(y) \sum_{n = -\infty}^{+\infty} \delta(t - n\tau) \qquad z > 0$$

$$\frac{\partial T}{\partial t} = D_{-} \nabla^{2} T \qquad z < 0 \qquad (11)$$

where τ is the interval between the pulses. The time dependence of the last term can be expressed in terms of its harmonic components as a frequency comb

$$\sum_{n=-\infty}^{+\infty} \delta(t-n\tau) = \frac{1}{\tau} \sum_{n=-\infty}^{+\infty} e^{-i2\pi mt/\tau} \quad (12)$$

and we can use Eq.(1) for each harmonic component separately in linear response. If $\tau \to 0$ only the m=0 zero-frequency part of the temperature profile survives, since $\frac{2\pi m}{\tau} \to \infty$ for any $m \neq 0$,i.e. $\kappa_{\pm} \to \infty$. There is a localized temperature variation near the source, out to a thermal distance $\kappa_{+}^{-1} \sim \sqrt{\tau}$. (The zero-frequency part of the temperature profile has an infinite amplitude, but that is only because the average rate of heat injection implied by Eq.(12) is infinite; if a factor of τ is introduced on both sides to prevent this, the resultant temperature profile has a finite amplitude.)

In the other limit, when $\tau \to \omega$ the heating due to a pulse dissipates completely before the next pulse is applied. The right hand side of Eq.(12) is replaced with a Fourier integral, $(2\pi)^{-1} \int \exp(-i\omega t) \, d\omega$ and the answer obtained from Eq.(1) can be integrated over time.

3. Numerical simulations

In order to visualize the effect of a membrane on the heat propagation in more detail, we performed temperature simulations using an open source, MATLAB integrated three dimensional Monte Carlo Light Transport Solver with Heat Diffusion and Tissue Damage⁴³. Although this is an expansive tool with many modules, the heat propagation module in a three-dimensional geometry was modified to match the scenario of a point source with a fixed distance away from a thin two-dimensional layer. The thermal properties of the surrounding medium 1 are set to those of water while the properties of the thin layer (medium 2) are set to those commonly cited for lipid bilayers. The point source is visualized as a 20 nm absorber (medium 3), as seen in Fig. 1, with similar thermal properties as water. The simulation

parameters are listed in Table 1. Defining the thermal diffusivity as $D = \frac{\kappa}{\rho C v}$, where κ represents the thermal conductivity, ρ the density and C_v the volumetric heat capacity, where the latter value in lipid bilayers is roughly half that of pure water. Considering the presence of transmembrane proteins, the diffusivity is expected to have a 2.6 fold decrease due to an increased heat capacity³¹. A comparison between lipid bilayers with and without transmembrane proteins is presented in the Supplementary material, and in the main text we will focus on pure lipid bilayers.

	Thermal conductivity κ (W · m ⁻¹ · K ⁻¹)	Volumetric Heat Capacity C_{ν} (J · m ⁻³ · K ⁻¹)	Density ρ $(g \cdot m^{-3})$	Thermal diffusivity D $(m^2 \cdot s^{-1})$	Absorption coefficient (cm ⁻¹)
Medium 1 - Water	0.6	4.2 · 10 ⁻⁶	1 · 10 ⁻⁶	14.2 · 10 ⁻⁸	0
Medium 2 – Lipid Bilayer	0.25	$2.7 \cdot 10^{-6}$ 44,45	$1 \cdot 10^{-6}$ 30	$7 \cdot 10^{-8}$	0
Medium 3 - Absorber	0.6	4.2 · 10 ⁻⁶	1 · 10 ⁻⁶	$14.2 \cdot 10^{-8}$	3· 10 ³

Table 1: Thermal properties for the three media (water, lipid bilayer, absorber) in the simulation cuboid

The absorber is centered at coordinates (X, Y, Z) = (0, 0, 470 nm) while the membrane layer is set to have a thickness of 12 nm from Z = 500 - 512 nm (simulated cuboid in X from -500 to +500 nm with 10 nm steps, -500 to +500 nm with 10 nm steps in Y and from 0 to +1 μ m with 2nm steps for Z). In order to simulate a point source scenario, the absorber is the only medium with a significant non-zero absorption coefficient set at 3000 cm⁻¹, corresponding to standard values for water absorption in the mid-infrared regime. The point absorber is modeled by an artificial 20 nm beam focused at (0, 0, 470 nm), that matches the absorber diameter. The illumination is modulated in time with a fixed 5% duty cycle and a pulse peak power of 0.2 mW. It should be noted that the scaling of power is a linear system and thus different pulse peak power and beam intensity combinations are not expected to affect the rate of heat propagation. Also, because the power was kept low in both the simulation and experiments²², tissue damage is not a concern.

Figure 2 illustrates the temperature profiles at the end of the pulse in Figs. 2 (a), (d), (g) and (i) for different pulse durations for 500 ns, 50 ns, 5 ns and 0.5 ns. An abrupt change in slope is noticeable for the edge of the membrane at 500 nm for frequencies of 100 kHz, 1 MHz, 10 MHz and 100 MHz, corresponding to periods of 10 μ s, 1 μ s, 100 ns and 10 ns. Since an increase in frequency is associated with a shorter pulse duration, this results in a narrower temperature profile. Thus, at the highest frequency of 100 MHz, there is a smaller temperature rise ΔT at the membrane. In the Born approximation, the observed photothermal image is related to the temperature profile via Eq (13), and is related to the gradient of the dielectric constant or equivalently the gradient of the refractive index, as shown in Figures 2 (b), (e), (h) and (k) for 100 kHz, 1 MHz, 10 MHz and 100 MHz, respectively. By performing a Fourier Transform analysis, the frequency content of the signal at each specific pixel can be retrieved and the Fourier amplitude and phase signal for each pixel can be extracted, corresponding to the experimental lock-in detection.

Phase information can be a more sensitive probe than the amplitude to detect thermal gradients in membrane interfaces 22 . The corresponding phase images are shown in the third column of Figures 2 (c), (f), (i) and (I) for 100 kHz, 1 MHz, 10 MHz and 100 MHz, respectively (Fig S2). Here, the contrast from the heat propagation is enhanced at higher frequencies. The phase is defined as $\phi=\tan^{-1}\left(\frac{\mathrm{Im}(F_{\omega})}{\mathrm{Re}(F_{\omega})}\right)$, where F_{ω} corresponds to the complex Fourier Transform. Thus it does not depend on the strength of ΔT but rather on the relative contribution of the in-phase and out-of-phase signal contributions. The phase value presents itself as a mechanism for detecting time delays that can originate either from heat propagation in the medium or by a change in the inherent material thermal diffusivity.

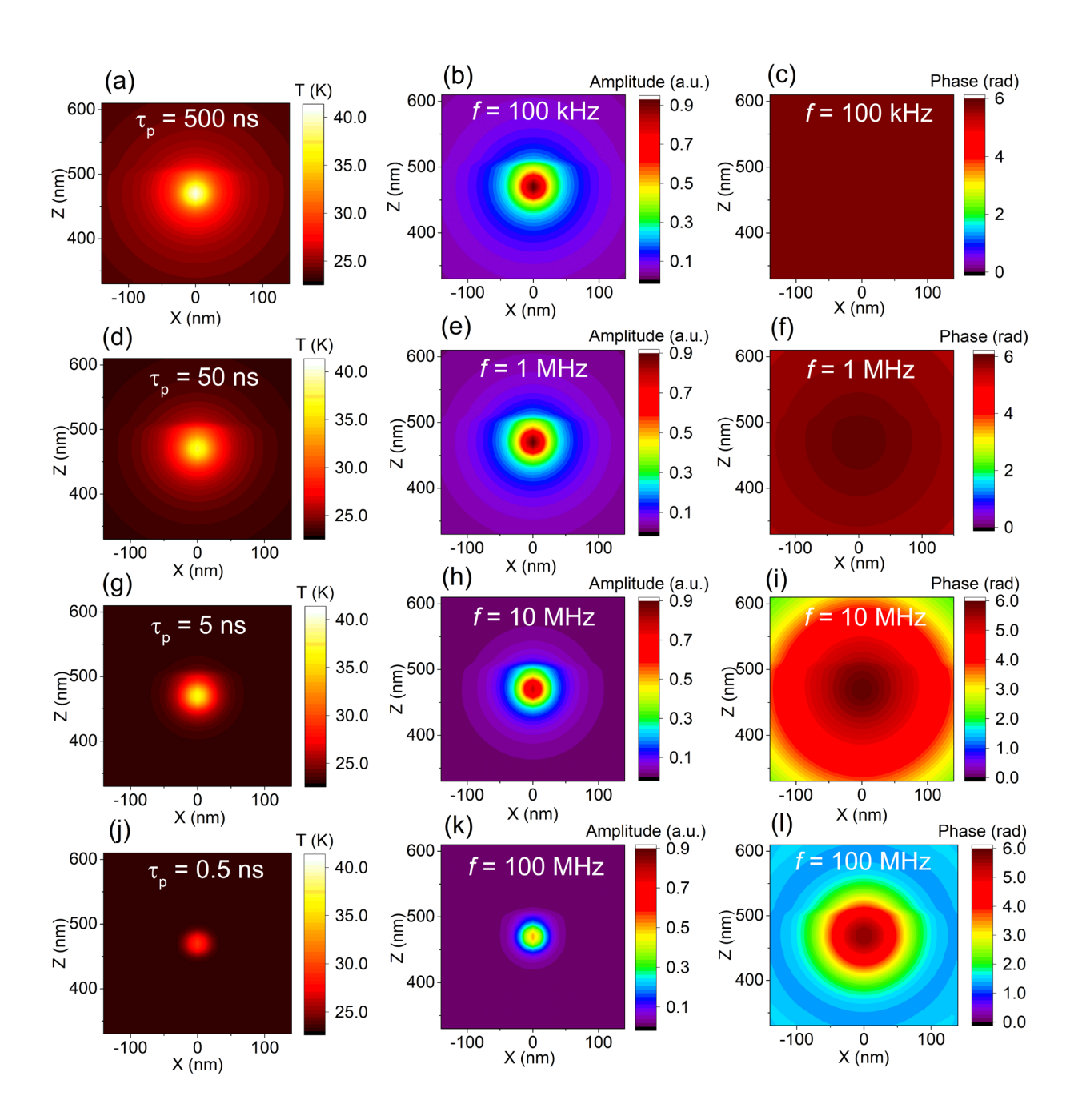


Figure 2: Temperature profiles at the time of maximum temperature rise corresponding to pulse durations of 500 ns, 50 ns, 5 ns and 0.5 ns are shown for repetition rates of (a) 100 kHz, (d) 1 MHz, (g) 10 MHz and (j) 100 MHz respectively, with slope changes detected at the membrane edge of z=500 nm. Amplitude images based on Fourier analysis are shown in the second column for (b) 100 kHz, (e) 1 MHz, (h) 10 MHz and (k) 100 MHz. Phase images from Fourier analysis are shown in the third column for (c) 100 kHz, (f) 1 MHz, (i) 10MHz and (l) 100 MHz where an enhanced contrast from membrane interface is noticeable with increasing frequency.

In order to study the effect of the membrane presence in heat propagation in more detail, the linescans across the amplitude (A) and phase (Φ) images in Figures 3 (a) and (b) are shown for all the simulated frequencies. The linescans are located at x =0 and the range for z is set from 488 to 524 nm. In Figure 3 (a), a change in slope is observed at the membrane edges at 500 nm as well as 512 nm. We can quantify the change in slope by performing a linear fit at the membrane region and a similar fit at the water regions between 488 and 500 nm (which we will refer to as Water A) and between 512 and 524 nm (which we will refer to as Water B). The values of the slopes are summarized in Table 1. Overall we report an overall decrease of the amplitude slope dA/dz at the membrane region with increasing frequencies from -17.9 μ m⁻¹ to -7.9 μ m⁻¹, corresponding to frequencies of 100 kHz and 100 MHz, respectively. It should be noted that the difference in dA/dz between the membrane and water regions is more pronounced when membrane is compared to water B than water A. When investigating the equivalent $d\Phi/dz$ values, an opposite trend is observed at which the slopes at the membrane are increasing with higher frequencies from -1.24 rad/ μ m to 68.5 rad/ μ m (Table 2). These results indicate stronger phase changes due to the presence of the membrane interface, providing an increased sensitivity compared to the amplitude profiles.

	dA/dz	dA/dz	dA/dz	dΦ/dz	dΦ/dz	dΦ/dz
	(µm ⁻¹)	(µm ⁻¹)	(µm ⁻¹)	(rad/μm)	(rad/μm)	(rad/μm)
	Water A	Membrane	Water B	Water A	Membrane	Water B
100 kHz	-16.4	-17.9	-4.4	-0.47	-1.24	-0.74
1 MHz	-16.3	-17.7	-4.3	-2.3	-5.75	-3.57
10 MHz	-15.5	-16.1	-3.6	-9.8	-21.2	-15.7
100 MHz	11	-7.9	-1	-41.6	-68.5	-68.2

Table 2: Slopes of linear fits at the three different regions defined as Water A (488-500 nm), Membrane (500-512 nm) and Water B (512-524 nm) for both Amplitude (dA/dz) as well as Phase ($d\Phi/dz$). Each row corresponds to a different frequency, including 100 kHz, 1 MHz, 10 MHz and 100 MHz.

The Kapitza length L_K is defined as the equivalent length of the fluid that would have the same thermal resistance as the membrane. To calculate L_K the membrane is first approximated as having zero width so that the temperature drop across it appears as a discontinuity (see Figure 3(c)). The linear fit of the temperature profile in the region Water B (dA/dz_{water-B}) is extrapolated backwards until it matches the temperature on the A-side of the membrane as shown in Fig 3(c). The length needed to achieve this is the Kapitza length L_K which is also called the *thermal resistance length*. The frequency dependence of L_K is shown in Figure 3 (d) for both the numerical results (open circles) as well as the analytical model (solid

circles) based on Equation 7. For the latter analytical values, the thermal resistance ρ was defined as the $\rho=\frac{d_m}{\kappa_m}$, where d_m corresponds to the membrane thickness of 12 nm, and κ_m to the thermal conductivity of lipid bilayers of 0.25 W·m⁻¹·K⁻¹, giving a thermal resistance of 48 · 10⁻⁹ m²·K·W⁻¹ or an equivalent thermal conductance of 20 MW·m⁻²·K⁻¹. Overall, as seen in Figure 3 (d), a 1.5 to 1.9 fold increase from 100 kHz to 100 MHz is reported, with L_k increasing from 41.5 nm to 79.1 nm and 45 nm to 67.5 nm corresponding to numerical and analytical values. The increase of L_k with higher frequency indicates a higher sensitivity on thermal resistance effects at the membrane interface when modulating at higher frequency. However as mentioned earlier, the narrower temperature profile inherent to 100 MHz naturally results in lower signal in the vicinity of the membrane which can inhibit detection. Thus, we suggest that it is more beneficial to investigate the phase component as it is insensitive to intensity variations and can provide higher contrast as demonstrated in Figure 2. The frequency dependence of the phase difference at z=500 nm with and without the membrane is shown in Figure 3 (e). A substantial increase is seen when the frequency is increased from 100 kHz to 100 MHz. We also present in the Supplementary Material enhanced phase contrast at 100 MHz when comparing the presence of different resistive interfaces, specifically a pure lipid bilayer, with a lipid bilayer containing transmembrane proteins.

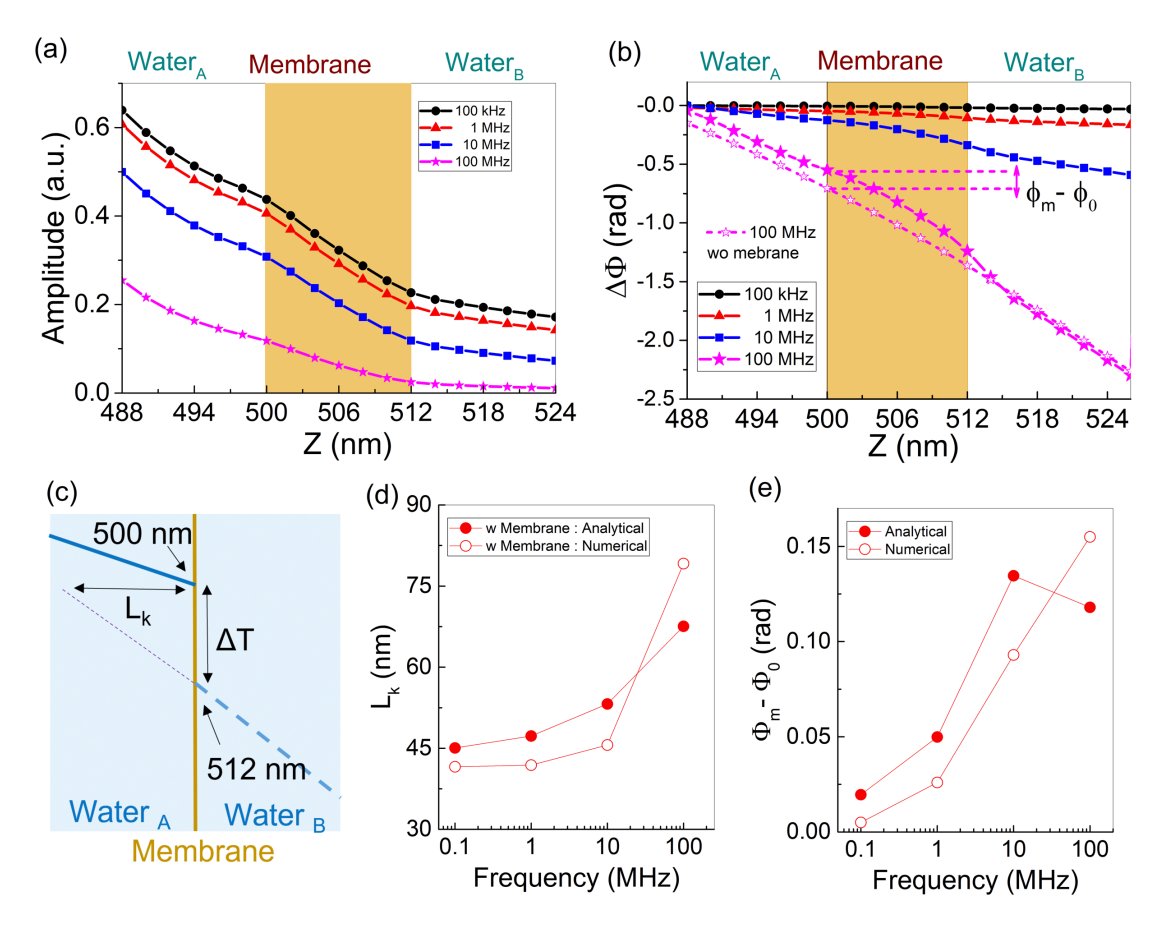


Figure 3: Linescans from amplitude (a) and phase (b) images at 100 kHz (circle), 1 MHz (triangle), 10 MHz (square) and 100 MHz (star), between 488 and 524 nm, from the numerical results. The membrane region is highlighted in dark yellow between 500 and 512 nm. (c) Schematic illustrating the Kapitza length (L_k). (d) The frequency dependence of L_k from the analytical model (solid red circles) and from the numerical simulation (open red circles) is shown. (e) Frequency dependence of the phase difference $\Phi_m - \Phi_0$ at z=500 nm for the analytical model (solid

red circles) and from the numerical simulation (open circles). Φ_m is the phase observed in the presence of the membrane, whereas Φ_0 is the reference phase in the absence of the membrane.

Our results show that as the modulation frequency rises, the sensitivity of the phase gradient increases, consistent with the analytical model. Molecular Dynamics simulations and thermoreflectance studies show that the Kapitza resistance associated with bilayer membranes $R_K \equiv \frac{1}{G}$ with a thermal conductance in the range of $G \sim 150-250~\mathrm{MW}\cdot\mathrm{m}^{-2}\cdot\mathrm{K}^{-1}$ 46 , 47 , 48 corresponds to a Kapitza length for hydrophilic surface in the 3-6 nm range. Thermoreflectance measurements reported previously require heating of a gold-coated substrate in contact with the membrane. Such a geometry is impossible in a cell membrane. Our results show for the first time how label-free photothermal methods with sufficiently high modulation frequency can probe the presence of interfacial membrane resistance. Recent nanosecond-scale measurements 19 and high frequency widefield setups 15 have demonstrated the feasibility of high frequency experiments with high harmonic demodulation in the MHz regime. Thus, the use of high-speed electronics and post processing can potentially in the future enable a direct experimental measurement of the Kapitza length and Kapitza resistance utilizing the sensitivity of higher frequency components.

4. Discussion

The expressions we have obtained so far have been for $T_{\omega}(\mathbf{q}_{\perp},z)$ and $T(\mathbf{q}_{\perp},z,t)$. It is straightforward to perform an inverse Fourier transform on these functions to obtain $T(\mathbf{r},t)$. However, if the temperature profile is measured using elastic light scattering as in photothermal microscopy, the change in the local dielectric constant $\delta\epsilon(\mathbf{r},t)$ that results from the temperature increase $T(\mathbf{r},t)$ is small and linearly proportional to $T(\mathbf{r},t)$ with $\delta\epsilon(\mathbf{r},t) \propto T(\mathbf{r},t)$. The Born approximation can then be used. Then the differential scattering cross section as a function of direction is given by

$$\frac{d\sigma}{d\Omega} = \frac{k^4}{(4\pi\varepsilon_0)^2} \left| \int d\mathbf{r} \exp[i(\mathbf{k}_{\rm in} - \mathbf{k}_{out}) \cdot \mathbf{r}] \mathbf{e}_{\rm out}^* \cdot \mathbf{e}_{\rm in} \, \delta\epsilon(\mathbf{r}, t) \right|^2$$
(13)

where $\mathbf{e}_{\mathrm{out}}$, \mathbf{e}_{in} are the polarization vectors and $\mathbf{k}_{\mathrm{out}}$, \mathbf{k}_{in} are wavevectors respectively for the incoming light and the scattered light. (Here we have assumed that the time dependence of the temperature is sufficiently slow that we do not need to use the retarded time in $\delta \epsilon(\mathbf{r},t)$.) Thus we see that the scattering cross section effectively measures the temperature profile $T(\mathbf{q},t)$ with $\mathbf{q}=\mathbf{k}_{\mathrm{out}}-\mathbf{k}_{\mathrm{in}}$. Instead of obtaining $T(\mathbf{r},t)$ from $T(\mathbf{q}_{\perp},z,t)$ we have to Fourier transform in the z-direction, too, to obtain $T_{\mathbf{q}}(\mathbf{q}_{\perp},q_z,t)=T(\mathbf{q},t)$, where $\mathbf{q}=\mathbf{q}_{\perp}+q_z\mathbf{\hat{z}}$. As the direction in which the scattering cross section is measured is varied, the magnitude and the direction of $\mathbf{q}=\mathbf{k}_{\mathrm{out}}-\mathbf{k}_{\mathrm{in}}$ change. As the angle α between the normal to the membrane and $\mathbf{k}_{\mathrm{out}}-\mathbf{k}_{\mathrm{in}}$ is varied, $q_z=q\cos\alpha$ and $|\mathbf{q}_{\perp}|=q\sin\alpha$ both change. The formulation here has the advantage of directly relating the photothermal image to the temperature profile.

For sinusoidal forcing, with the temperature profile obtained in Section 2.1 (Eq 7-10), we obtain

$$T_{\omega}(\mathbf{q}) = \frac{A}{\kappa - iq_z} + \frac{F}{\kappa_+ + iq_z} + \frac{1}{2D_+\kappa_+} \left[\frac{e^{-iq_z a}}{\kappa_+ + iq_z} + \frac{e^{-iq_z a} - e^{-\kappa_+ a}}{\kappa_+ - iq_z} \right]$$
(14)

When the media on the two sides of the membrane are the same, e.g. both aqueous, the calculations simplify considerably. Since $C_+=C_-\equiv C$ and $D_+=D_-\equiv D$ from Eq (8) we get $\kappa_+=\kappa_-\equiv \kappa$. The Kapitza length for the membrane is the same on either side of the membrane: $L_K=\rho CD$. Eq (1) then reduces to

$$A = \frac{1}{D\kappa} \cdot \frac{1}{2 + \kappa L_K} e^{-\kappa a}$$
$$F = \frac{1}{2} A L_K \kappa \tag{15}$$

Eq (14) for $T_{\omega}(\mathbf{q})$ now reduces to

$$T_{\omega}(\mathbf{q}) = \frac{1}{D(\kappa^2 + q_z^2)} \left[e^{-iq_z a} - i \frac{L_K q_z}{2 + \kappa L_K} e^{-\kappa a} \right]$$
(16)

For the second term to be comparable to the first, and also sensitive to the Kapitza length L_K , we need that $q_z L_K$ should not be too small (compared to 1), and κL_K and κa should not be too large. (Formally, the condition on κa is a condition on $\text{Re}[\kappa]a$, but we see that this does not make a difference.) If the Kapitza length L_K is approximately 10 nm, and a is approximately 100 nm, then $|\kappa a| > |\kappa L_K|$. The conditions to be satisfied are that $|\kappa|a$ should not be too large, while $L_K q_z$ should not be too small.

With a probe wavelength $\lambda_{probe}=1550~\mathrm{nm}$ and with $q=|\mathbf{k}_{\mathrm{out}}-\mathbf{k}_{\mathrm{in}}|=2k\sin\frac{\theta}{2}~$ in the elastic scattering regime, we have $q\approx 0.007~\mathrm{nm}^{-1}$ for $\theta\approx\frac{2\pi}{3}$. Now $\kappa^2=q_\perp^2-i\omega/D$ where $\omega=2\pi\nu$ is the pump laser forcing frequency that ranges in experiments from $\sim 100~\mathrm{kHz}$ to the MHz range. With $D=1.4\times10^{-7}~\mathrm{m^2\cdot s^{-1}}$ if $q_\perp\approx q_z\approx q/\sqrt{2}$ we see that $q_\perp^2\approx 2.5\times10^{-5}~\mathrm{nm^{-2}}$. At a pump modulation frequency of $100~\mathrm{kHz}$ $\frac{\omega}{D}\approx 4.5\times10^{-6}~\mathrm{nm^{-2}}$ and q_\perp^2 is much larger than $\frac{\omega}{D}$. Therefore $\kappa\approx\mathrm{Re}[\kappa]=q_\perp$. Under these conditions, the second term $\frac{L_Kq_z}{2+\kappa L_K}e^{-\kappa a}\approx 0.015$ compared to the first. The strength of the signal can be increased further if q is increased by increasing k or θ as long as the orientation of the membrane is such that $q_z\gg q_\perp$. (Recall that q_z is the component of \mathbf{q} normal to the membrane and q_\perp is the component in the plane of the membrane.) As an example, for a shorter wavelength probe $\lambda=530~\mathrm{nm}$, keeping the same angle $\theta\approx\frac{2\pi}{3}$ and with an angle between \mathbf{q} and the membrane normal of about 15° , the ratio of the second term to the first term increases to 0.058, readily detectable with sensitive phase lock methods.

Ge et al 46 have reported measurements at optical wavelengths that are sensitive to such small length scales associated with the Kapitza length. We remark that in the Thermoreflectance measurements of Ge et al, the membrane was in contact with a large metallic substrate, with an effective $a \leq 1$ nm. In living cells, it is difficult to place a large substrate in contact. Our work shows that if an absorbing nanoparticle is placed close to the membrane, the prospects for measuring the Kapitza length in a membrane vesicle become much more promising even with relatively long wavelength probes.

5. Extension to 3D: Spherical Membrane

If the cell is small, it is not a reasonable approximation to treat the cell membrane as an infinite plane. Another case that can be solved analytically is that of a spherical membrane. We assume that the heating source is outside the sphere instead of inside it, and that the heating is sinusoidal. (It is easy to extend the discussion here to cover the case when the heating source is pulsed and is inside the sphere.) Without loss of generality, we assume that the heating source is on the z axis, i.e. at $\theta=0$ in spherical polar coordinates.

We express the temperature as $T(r,\theta,t)=e^{-i\omega t}\sum_{l}R_{l}(r)P_{l}(\cos\theta)$ and write the δ -function in Eq.(1) as

$$\delta(z-a)\delta(x)\delta(y) = \sum_{l} \frac{2l+1}{4\pi r^2} \delta(r-a) P_l(\cos\theta) \quad \text{Eq (14)}$$

Eqs(1) are then equivalent to

$$\frac{d}{dr}r^2 \frac{dR_l}{dr} + \left[\frac{i\omega}{D_+}r^2 - l(l+1)\right] R_l(r) = -\frac{2l+1}{4\pi}\delta(r-a) \qquad r > r_0$$

$$\frac{d}{dr}r^2 \frac{dR_l}{dr} + \left[\frac{i\omega}{D_-}r^2 - l(l+1)\right] R_l(r) = 0 \qquad r < r_0$$
(15)

where r_0 is the radius of the sphere. The distance between the heating source and the membrane is now equal to $a-r_0$ instead of a; we could replace a with $a+r_0$ to keep the same distance that we had for an infinite flat membrane, at the expense of cluttering the formulas for the spherical case.

The solution to these equations is of the form

$$R_{l}(r) = \begin{cases} A_{1}j_{l}(\alpha_{-}r) & r < r_{0} \\ A_{2}j_{l}(\alpha_{+}r) + A_{3}h_{l}^{(1)}(\alpha_{+}r) & r_{0} < r < a \quad \text{Eq}(16) \\ A_{4}h_{l}^{(1)}(\alpha_{+}r) & a < r \end{cases}$$

where

$$\alpha_{\pm} = (1+i)\sqrt{\frac{\omega}{2D_{\pm}}}$$
 Eq (17)

We have chosen the solution that is not divergent at r=0, and is outward propagating (together with an exponential decay) as $r \to \infty$.

Matching solutions at r = 0, and r = a, we have

$$\begin{split} A_2 j_l(\alpha_+ a) + A_3 h_l^{(1)}(\alpha_+ a) &= A_4 h_l^{(1)}(\alpha_+ a) \\ A_2 j_l'(\alpha_+ a) + A_3 {h_l^{(1)}}'(\alpha_+ a) &= A_4 {h_l^{(1)}}'(\alpha_+ a) + \frac{(2l+1)}{4\pi\alpha_+ a^2} \\ D_+ C_+ \alpha_+ \left[A_2 j_l'(\alpha_+ r_0) + A_3 {h_l^{(1)}}'(\alpha_+ r_0) \right] &= D_- C_- \alpha_- A_1 j_l'(\alpha_- r_0) \end{split}$$

$$\frac{1}{\rho} \left[A_2 j_l(\alpha_+ r_0) + A_3 h_l^{(1)}(\alpha_+ r_0) - A_1 j_l(\alpha_- r_0) \right] = D_- C_- \alpha_- A_1 j_l'(\alpha_- r_0)$$
 Eq (18)

These equations can be solved numerically for any value of l if physical quantities such as ω , D_{\pm} are known. When the radius of the sphere is large or equivalently in the small curvature limit, the asymptotic behavior of the spherical Bessel functions give results are identical to Eq (9-10), providing support for the infinite plane approximation. The analytical approach here provides derived Green functions in a Spherical geometry. Fourier transforming the solution provides a full 3D image in the first Born approximation.

Conclusion

The analytical model for light scattering in the far field in the first-Born approximation provides insight into thermal transport near a cell membrane that divides a complex system into two topologically distinct half spaces. The derived Green function leads to the reconstruction of a full 3D image with photothermal contrast obtained using both amplitude and phase detection of periodic excitations. Important fundamental parameters including the Kapitza length and Kapitza resistance can be derived from experiments with sufficiently high frequency modulation. Our work provides motivation for additional experimental studies at high frequency modulation and heterodyne detection and spur between the thermal imaging community and theoretical molecular dynamics simulations community, with a view to under the Kapitza parameters and related thermal transport properties in lipid membrane systems.

Acknowledgments

We thank Prof LD Ziegler, Prof Ji-Xin Cheng and their groups for discussions, and acknowledge support from the National Institutes of Health (123456 and R01GM142012); and the National Science Foundation (NSF ECCS-1846659).

Ethical Statement:

Funding: Support is acknowledged from the National Institutes of Health (123456 and R01GM142012); and the National Science Foundation (NSF ECCS-1846659)

Conflict of Interest: The authors report no Conflict of Interest

Informed consent: N/A (no animal or human studies)

Author contributions: PDS carried out the simulations, supervised by MYS and assisted by SE. ON worked out the theory. SE and MKH drafted the manuscript and all authors contributed to the final writing.

References:

- ¹ M. Bertolotti, and R. Li Voti, "A note on the history of photoacoustic, thermal lensing, and photothermal deflection techniques," Journal of Applied Physics **128**(23), 230901 (2020).
- ² S. Berciaud, D. Lasne, G.A. Blab, L. Cognet, and B. Lounis, "Photothermal heterodyne imaging of individual metallic nanoparticles: Theory versus experiment," Phys. Rev. B **73**(4), 045424 (2006).
- ³ S. Berciaud, L. Cognet, G.A. Blab, and B. Lounis, "Photothermal Heterodyne Imaging of Individual Nonfluorescent Nanoclusters and Nanocrystals," Phys. Rev. Lett. **93**(25), 257402 (2004).
- ⁴ S. Adhikari, P. Spaeth, A. Kar, M.D. Baaske, S. Khatua, and M. Orrit, "Photothermal Microscopy: Imaging the Optical Absorption of Single Nanoparticles and Single Molecules," ACS Nano **14**(12), 16414–16445 (2020).
- ⁵ A. Gaiduk, M. Yorulmaz, P.V. Ruijgrok, and M. Orrit, "Room-temperature detection of a single molecule's absorption by photothermal contrast," Science **330**(6002), 353–356 (2010).
- ⁶ A. Mertiri, H. Altug, M.K. Hong, P. Mehta, J. Mertz, L.D. Ziegler, and S. Erramilli, "Nonlinear Midinfrared Photothermal Spectroscopy Using Zharov Splitting and Quantum Cascade Lasers," ACS Photonics **1**(8), 696–702 (2014).
- ⁷ A. Totachawattana, M.K. Hong, S. Erramilli, and M.Y. Sander, "Multiple bifurcations with signal enhancement in nonlinear mid-infrared thermal lens spectroscopy," Analyst **142**(11), 1882–1890 (2017).
- ⁸ I.M. Pavlovetc, E.A. Podshivaylov, R. Chatterjee, G.V. Hartland, P.A. Frantsuzov, and M. Kuno, "Infrared photothermal heterodyne imaging: Contrast mechanism and detection limits," Journal of Applied Physics **127**(16), 165101 (2020).
- ⁹ D. Zhang, C. Li, C. Zhang, M.N. Slipchenko, G. Eakins, and J.-X. Cheng, "Depth-resolved mid-infrared photothermal imaging of living cells and organisms with submicrometer spatial resolution," Science Advances, (2016).
- ¹⁰ Z. Li, K. Aleshire, M. Kuno, and G.V. Hartland, "Super-Resolution Far-Field Infrared Imaging by Photothermal Heterodyne Imaging," J. Phys. Chem. B **121**(37), 8838–8846 (2017).
- ¹¹ K. Aleshire, I.M. Pavlovetc, R. Collette, X.-T. Kong, P.D. Rack, S. Zhang, D.J. Masiello, J.P. Camden, G.V. Hartland, and M. Kuno, "Far-field midinfrared superresolution imaging and spectroscopy of single high aspect ratio gold nanowires," PNAS **117**(5), 2288–2293 (2020).
- ¹² Y. Zhang, C. Yurdakul, A.J. Devaux, L. Wang, X.G. Xu, J.H. Connor, M.S. Ünlü, and J.-X. Cheng, "Vibrational Spectroscopic Detection of a Single Virus by Mid-Infrared Photothermal Microscopy," Anal. Chem. **93**(8), 4100–4107 (2021).
- ¹³ H. Zong, C. Yurdakul, Y. Bai, M. Zhang, M.S. Ünlü, and J.-X. Cheng, "Background-Suppressed High-Throughput Mid-Infrared Photothermal Microscopy via Pupil Engineering," ACS Photonics **8**(11), 3323–3336 (2021).
- ¹⁴ Y. Bai, D. Zhang, L. Lan, Y. Huang, K. Maize, A. Shakouri, and J.-X. Cheng, "Ultrafast chemical imaging by widefield photothermal sensing of infrared absorption," Science Advances, (2019).
- ¹⁵ E.M. Paiva, and F.M. Schmidt, "Ultrafast Widefield Mid-Infrared Photothermal Heterodyne Imaging," Anal. Chem. **94**(41), 14242–14250 (2022).
- ¹⁶ M. Tamamitsu, K. Toda, H. Shimada, T. Honda, M. Takarada, K. Okabe, Y. Nagashima, R. Horisaki, and T. Ideguchi, "Label-free biochemical quantitative phase imaging with mid-infrared photothermal effect," Optica, OPTICA **7**(4), 359–366 (2020).
- ¹⁷ H.M.L. Robert, K. Holanová, Ł. Bujak, M. Vala, V. Henrichs, Z. Lánský, and M. Piliarik, "Fast photothermal spatial light modulation for quantitative phase imaging at the nanoscale," Nat Commun **12**(1), 2921 (2021).
- ¹⁸ Y. Zhang, H. Zong, C. Zong, Y. Tan, M. Zhang, Y. Zhan, and J.-X. Cheng, "Fluorescence-Detected Mid-Infrared Photothermal Microscopy," J. Am. Chem. Soc. **143**(30), 11490–11499 (2021).

- ¹⁹ J. Yin, L. Lan, Y. Zhang, H. Ni, Y. Tan, M. Zhang, Y. Bai, and J.-X. Cheng, "Nanosecond-resolution photothermal dynamic imaging via MHZ digitization and match filtering," Nat Commun **12**(1), 7097 (2021).
- ²⁰ V.P. Zharov, "Ultrasharp nonlinear photothermal and photoacoustic resonances and holes beyond the spectral limit," Nature Photon **5**(2), 110–116 (2011).
- ²¹ P.D. Samolis, and M.Y. Sander, "Phase-sensitive lock-in detection for high-contrast mid-infrared photothermal imaging with sub-diffraction limited resolution," Opt. Express, OE **27**(3), 2643–2655 (2019).
- ²² P.D. Samolis, P.D. Samolis, D. Langley, D. Langley, B.M. O'Reilly, B.M. O'Reilly, Z. Oo, Z. Oo, G. Hilzenrat, G. Hilzenrat, S. Erramilli, S. Erramilli, S. Erramilli, A.E. Sgro, A.E. Sgro, A.E. Sgro, S. McArthur, S. McArthur, M.Y. Sander, M.Y. Sander, M.Y. Sander, and M.Y. Sander, "Label-free imaging of fibroblast membrane interfaces and protein signatures with vibrational infrared photothermal and phase signals," Biomed. Opt. Express, BOE **12**(1), 303–319 (2021).
- ²³ K. Chen, B. Song, N.K. Ravichandran, Q. Zheng, X. Chen, H. Lee, H. Sun, S. Li, G.A.G.U. Gamage, F. Tian, Z. Ding, Q. Song, A. Rai, H. Wu, P. Koirala, A.J. Schmidt, K. Watanabe, B. Lv, Z. Ren, L. Shi, D.G. Cahill, T. Taniguchi, D. Broido, and G. Chen, "Ultrahigh thermal conductivity in isotope-enriched cubic boron nitride," Science, (2020).
- ²⁴ R. Legrand, M. Abi Ghanem, L. Plawinski, M.-C. Durrieu, B. Audoin, and T. Dehoux, "Thermal microscopy of single biological cells," Appl. Phys. Lett. **107**(26), 263703 (2015).
- ²⁵ G. Baffou, H. Rigneault, D. Marguet, and L. Jullien, "A critique of methods for temperature imaging in single cells," Nat Methods **11**(9), 899–901 (2014).
- ²⁶ S. Sotoma, C. Zhong, J.C.Y. Kah, H. Yamashita, T. Plakhotnik, Y. Harada, and M. Suzuki, "In situ measurements of intracellular thermal conductivity using heater-thermometer hybrid diamond nanosensors," Science Advances, (2021).
- 27 K. Okabe, and S. Uchiyama, "Intracellular thermometry uncovers spontaneous thermogenesis and associated thermal signaling," Commun Biol **4**(1), 1–7 (2021).
- ²⁸ K. Okabe, N. Inada, C. Gota, Y. Harada, T. Funatsu, and S. Uchiyama, "Intracellular temperature mapping with a fluorescent polymeric thermometer and fluorescence lifetime imaging microscopy," Nat Commun **3**(1), 705 (2012).
- ²⁹ A.L. Garner, M. Deminsky, V. Bogdan Neculaes, V. Chashihin, A. Knizhnik, and B. Potapkin, "Cell membrane thermal gradients induced by electromagnetic fields," Journal of Applied Physics **113**(21), 214701 (2013).
- ³⁰ T.(中野雄大) Nakano, G.(菊川豪太) Kikugawa, and T.(小原拓) Ohara, "A molecular dynamics study on heat conduction characteristics in DPPC lipid bilayer," J. Chem. Phys. **133**(15), 154705 (2010).
- ³¹ J. Gómez, V.J. Hilser, D. Xie, and E. Freire, "The heat capacity of proteins," Proteins: Structure, Function, and Bioinformatics **22**(4), 404–412 (1995).
- 32 W. Tian, M. Lin, K. Tang, J. Liang, and H. Naveed, "High-resolution structure prediction of β -barrel membrane proteins," PNAS **115**(7), 1511–1516 (2018).
- ³³ A. Lervik, F. Bresme, S. Kjelstrup, D. Bedeaux, and J.M. Rubi, "Heat transfer in protein–water interfaces," Phys. Chem. Chem. Phys. **12**(7), 1610–1617 (2010).
- ³⁴ S. Youssefian, N. Rahbar, C.R. Lambert, and S. Van Dessel, "Variation of thermal conductivity of DPPC lipid bilayer membranes around the phase transition temperature," Journal of The Royal Society Interface **14**(130), 20170127 (2017).
- ³⁵ A.R.N. Bastos, C.D.S. Brites, P.A. Rojas-Gutierrez, C. DeWolf, R.A.S. Ferreira, J.A. Capobianco, and L.D. Carlos, "Thermal Properties of Lipid Bilayers Determined Using Upconversion Nanothermometry," Advanced Functional Materials **29**(48), 1905474 (2019).
- ³⁶ O.S. Andersen, and R.E. Koeppe, "Bilayer Thickness and Membrane Protein Function: An Energetic Perspective," Annual Review of Biophysics and Biomolecular Structure **36**(1), 107–130 (2007).

- ³⁷ V.P. Zharov, and D.O. Lapotko, "Photothermal imaging of nanoparticles and cells," IEEE Journal of Selected Topics in Quantum Electronics **11**(4), 733–751 (2005).
- ³⁸ D.Y. Tzou, "The generalized lagging response in small-scale and high-rate heating," International Journal of Heat and Mass Transfer **38**(17), 3231–3240 (1995).
- ³⁹ Shomali, Z., Kovács, R., Ván, P., Kudinov, I. V., Ghazanfarian, J. "Lagging heat models in thermodynamics and bioheat transfer: a critical review," Continuum Mechanics and Thermodynamics **34**(3), 637–679 (2022).
- ⁴⁰ N. Horny, M. Chirtoc, A. Fleming, G. Hamaoui, and H. Ban, "Kapitza thermal resistance studied by high-frequency photothermal radiometry," Appl. Phys. Lett. **109**(3), 033103 (2016).
- ⁴¹ Y. Zhang, "Generalized dual-phase lag bioheat equations based on nonequilibrium heat transfer in living biological tissues," International Journal of Heat and Mass Transfer **52**(21), 4829–4834 (2009).
- ⁴² T. Nakano, G. Kikugawa, and T. Ohara, "Molecular Heat Transfer in Lipid Bilayers With Symmetric and Asymmetric Tail Chains," Journal of Heat Transfer **135**(061301), (2013).
- ⁴³ D. Marti, R.N.N. Aasbjerg, P.E.E. Andersen, and A.K.K. Hansen, "MCmatlab: an open-source, user-friendly, MATLAB-integrated three-dimensional Monte Carlo light transport solver with heat diffusion and tissue damage," JBO **23**(12), 121622 (2018).
- ⁴⁴ P.F. Almeida, F.E. Carter, K.M. Kilgour, M.H. Raymonda, and E. Tejada, "Heat Capacity of DPPC/Cholesterol Mixtures: Comparison of Single Bilayers with Multibilayers and Simulations," Langmuir **34**(33), 9798–9809 (2018).
- ⁴⁵ A. Blume, "Apparent molar heat capacities of phospholipids in aqueous dispersion. Effects of chain length and head group structure," (1983).
- ⁴⁶ Z. Ge, D.G. Cahill, and P.V. Braun, "Thermal Conductance of Hydrophilic and Hydrophobic Interfaces," Phys. Rev. Lett. **96**(18), 186101 (2006).
- M. Nakano, Y. Arai, I. Kotera, K. Okabe, Y. Kamei, and T. Nagai, "Genetically encoded ratiometric fluorescent thermometer with wide range and rapid response," PLOS ONE 12(2), e0172344 (2017).
 M. Suzuki, and T. Plakhotnik, "The challenge of intracellular temperature," Biophys Rev 12(2), 593–600 (2020).